

Resonant Raman scattering of electrons in quantum wells: Identification of elementary excitations

A. A. P. Silva*

Departamento de Física, Universidade Federal de Mato Grosso do Sul, 79070-900 Campo Grande, MS, Brazil

Áurea R. Vasconcellos and Roberto Luzzi†

Instituto de Física Gleb Wataghin, Universidade Estadual de Campinas—Unicamp, 13083-970 Campinas, SP, Brazil

(Received 25 October 2005; revised manuscript received 13 January 2006; published 12 June 2006)

Inelastic scattering of light by electrons in a quantum well was studied. We considered the resonant Raman scattering associated with intersubband electronic excitations. Evidence is provided that when the two lowest subbands are considered four types of excitations are present. They give rise to two scattering lines associated with single-particle excitations and another two associated with collective charge-density excitations, while spin-density excitations are not considered. The shape of the Raman spectrum strongly depends on several characteristics in the experiment, namely, the quantum well width, the concentration of the carriers, many-body effects, the temperature, and, mainly, the momentum-transfer dependent on the laser-photon frequency and the experimental geometry. Particular experimental results are satisfactorily described.

DOI: [10.1103/PhysRevB.73.235320](https://doi.org/10.1103/PhysRevB.73.235320)

PACS number(s): 78.67.De, 73.21.Fg, 74.78.Fk, 67.40.Db

I. INTRODUCTION

Further developments in present day frontier technologies in the area of electronics and optoelectronics require an ever-decreasing size of devices, and an associated functioning on ever-smaller time scales. This leads to dealing with small dimension systems, such as quasi-two-dimensional ones (as in the case of quantum wells), signifying that carriers have discrete energy levels in one spatial dimension, but are free to move in two spatial dimensions; quasi-one-dimensional ones (so-called quantum wires), meaning that carriers are free to move in one spatial dimension, but have discrete energy levels in two spatial dimensions; and quasi-zero-dimensional ones (so-called quantum dots and columns) when the carriers have discrete energy levels in the three spatial dimensions.

These three cases of low-dimensional systems have been investigated by means of resonant Raman scattering. Sirenko *et al.*¹ report resonant Raman scattering in nanostructures with InP quantum dots in an $\text{In}_{0.48}\text{Ga}_{0.52}\text{P}$ matrix: At resonant excitation with the quantum dot excitons, broad band peaks corresponding to acoustic and optical vibrations were observed. Sasseti *et al.*² considered interband collective electronic excitations in resonant Raman scattering of two-subband quantum wires. Finally, for nanometric quantum wells, an early work was carried out by Pinczuk *et al.*,³ while another study was done more recently by Unuma *et al.*⁴ In all these works, the collective electronic excitations were analyzed. It may also be noted that resonant Raman scattering is relevant to the realization of intersubband Raman lasers, involving the possibility of reaching the far-infrared region in an operation at room temperature.⁵ We consider here the case of a “quasi-two-dimensional” quantum well, present in a semiconductor heterostructure. Our aim was to determine the spectrum of elementary excitations in the electron system.

Such excitations can be recorded, as also in the case of three-dimensional bulk samples, in Raman scattering experiments (see, for example, Refs. 6–8). Here we consider the case of resonant scattering, which is experimentally discernible (from the background of the whole sample) in quantum wells (see, for example, Refs. 3 and 4), and restricted to that originating in charge-density fluctuations, not considering that due to spin-density fluctuations (which involves the mediation of spin-orbit interaction).

The influence of many-body effects associated with the Coulomb interaction (treated as usual in the random phase approximation) are recorded. This is manifested in two aspects: the correction of the electron band-energy levels, and the formation of collective states (charge-density waves). We clearly shown in the following sections that the spectrum of excitations (associated with transitions in the two lowest subbands) is composed of two types of single-particle excitations and two types of collective excitations (this is discussed in Appendix A). This resembles the case of a double plasma of electrons and holes in the bulk. In the latter case, two types of single-particle excitations are also present, along with two collective excitations consisting of the so-called acoustic and optical plasmon vibrational modes.^{9,10}

These four types of elementary excitations are recorded in the Raman spectrum, which shows the four corresponding bands. We demonstrate in this study the particularly important fact that such spectra may have a variety of forms consisting mainly of notable differences in relative intensity among the different lines and eventual disappearance of some lines. This is a consequence of the influence, on the one hand, of several characteristics of the system such as the width of the quantum well (QW), the influence of the Coulomb interaction, the concentration of carriers, and, on the other hand, of the experimental protocol, basically, the temperature, the frequency of the laser light, and the geometry modifying the momentum transfer, which has a large influ-

ence on the results. For these reasons, the different types of excitations have not been clearly identified in existing experimental measurements.

II. RESONANT RAMAN SCATTERING IN SINGLE QW

It has been stated that intersubband electronic excitations in QWs are strongly affected by many-body Coulomb interactions.¹¹ First, this is manifested in the single-particle elementary spectrum, where we recall that the single-particle energies depend on a discrete index (positive integers) l associated with the Bloch-band kinetic energy in the direction along the nanometric QW of length L_{QW} , and a two-dimensional wave vector, \mathbf{k}_{\perp} , associated with the free motion in the transverse section of the QW: for particles of mass m^* in an *ideal* QW we have the textbook expression

$$\varepsilon_l^0(\mathbf{k}_{\perp}) = l^2 \frac{\pi^2 \hbar^2}{2m^* L_{\text{QW}}^2} + \frac{\hbar^2 \mathbf{k}_{\perp}^2}{2m^*}, \quad (1)$$

with $l=1,2,\dots$ and where we have omitted the spin index. (In Sec. IV we discuss the question of the presence and influence of fractal-like structured boundaries.) However, in the excitation spectrum it is necessary to include the corrections to the Hartree-Fock approximation used in deriving the Bloch-band scheme (for example, Ref. 9). For transitions between subbands $l=1$ and $l=2$ and with wave vector change from \mathbf{k}_{\perp} to $\mathbf{k}_{\perp} + \mathbf{Q}$, we have

$$\varepsilon_2(\mathbf{k}_{\perp} + \mathbf{Q}) - \varepsilon_1(\mathbf{k}_{\perp}) = E_{21}(\mathbf{k}_{\perp}, \mathbf{Q}) + N_S(A_{21} - B_{21}), \quad (2)$$

where, in the usual single-electron approximation,

$$\begin{aligned} E_{21}(\mathbf{k}_{\perp}, \mathbf{Q}) &= \varepsilon_2^0(\mathbf{k}_{\perp} + \mathbf{Q}) - \varepsilon_1^0(\mathbf{k}_{\perp}) \\ &= \frac{3\pi^2 \hbar^2}{2m^* L_{\text{QW}}^2} + \frac{\hbar^2}{2m^*} \mathbf{Q} \cdot (2\mathbf{k}_{\perp} + \mathbf{Q}), \end{aligned} \quad (3)$$

$$A_{21} = \frac{1}{N_S} \sum_{l'} V_{2D}(\mathbf{Q}) [F_{22}^{l'l'}(\mathbf{Q}) f_2(\mathbf{k}_{\perp} + \mathbf{Q}) - F_{11}^{l'l'}(\mathbf{Q}) f_1(\mathbf{k}_{\perp})], \quad (4)$$

$$\begin{aligned} B_{21} &= \frac{1}{N_S} \sum_{l'} \delta_{\sigma\sigma'} [U_{2l'} F_{2l'}^{2l'}(\mathbf{Q}) f_2(\mathbf{k}_{\perp} + \mathbf{Q}) \\ &\quad - U_{1l'} F_{1l'}^{1l'}(\mathbf{Q}) f_1(\mathbf{k}_{\perp})], \end{aligned} \quad (5)$$

with N_S being the electron sheet-density, $N_S = nL_{\text{QW}}$ where n is the concentration of the mobile conduction band electrons in the n -doped sample; A and B are, respectively, the direct and exchange contributions originated in the Coulomb interaction in the Hartree-Fock approximation,^{12,13} which have for the electrons in the QW the expressions of Eqs. (4) and (5), following from a calculation in terms of the standard wave functions and energy levels.¹¹ The exchange contribution, we recall, involves only electrons with the same spin and the U 's are the exchange integrals (the s -type Landau's interaction strengths),¹³ $V_{2D}(\mathbf{Q}) = e^2/2\epsilon_0 Q S$ is the matrix el-

ement in plane-wave states of the Coulomb potential in 2D, where S is the area of the transverse (sheet) surface and $F_{mm'}^{mm'}(\mathbf{Q})$ is the quantity given in Ref. 14, namely

$$F_{mm'}^{mm'}(\mathbf{Q}) = \int_{-\infty}^{\infty} dz \int_{-\infty}^{\infty} dz' \varphi_m^*(z) \varphi_m(z) \varphi_{n'}^*(z') \varphi_{n'}(z') e^{-Q(z-z')}, \quad (6)$$

where $\varphi(z)$ is the contribution to the single-electron wave function corresponding to the states associated with the constrained z direction in the QW. Finally, $f_l(\mathbf{k}_{\perp})$ is the population of electrons in the state (l, \mathbf{k}_{\perp}) , i.e., Fermi-Dirac distributions with temperature T and chemical potential μ . The values of A and B can be obtained from the experimental data, as illustrated later on. Moreover, we use parabolic Bloch bands disregarding nonparabolicity effects which are not relevant for the scattering by charge density fluctuations here considered.

We proceed now to the calculation of the resonant Raman spectrum in scattering by the lowest ($1 \rightarrow 2$) intersubband electronic excitations in an n -doped single QW (experimental data in particular conditions are reported in Refs. 3 and 4). As described in Appendix B, the resonant Raman scattering is the one associated with the QW that is discernible from the background arising from the whole sample. It is, we recall, a second-order process involving double the $(\mathbf{A} \cdot \mathbf{p})$ contribution to the interaction of the electron with the radiation fields (incident and scattered), and with the laser photon energy approaching, or being slightly larger than, the value of the band gap which makes one of the energy denominators in the virtual intermediate state very small [cf. Eq. (B5)].

The scattering cross section for the events with excitation energy as given by Eq. (2)—i.e., transitions between subbands $l=1$ and $l=2$ with crystalline momentum transfer $\hbar\mathbf{Q}$ (see Appendix B)—is given by

$$\frac{d^2\sigma}{d\omega d\Omega} \sim [1 - e^{-\beta\hbar\omega}]^{-1} \text{Im} \left\{ \frac{F_{21}(\mathbf{Q}, \omega)}{1 + V_{2D}(\mathbf{Q}) F_{21}(\mathbf{Q}, \omega)} \right\}, \quad (7)$$

where Im stands for an imaginary part, and

$$F_{21}(\mathbf{Q}, \omega) = \sum_{\mathbf{k}_{\perp}} \frac{f_1(\mathbf{k}_{\perp}) - f_2(\mathbf{k}_{\perp} + \mathbf{Q})}{\varepsilon_2(\mathbf{k}_{\perp} + \mathbf{Q}) - \varepsilon_1(\mathbf{k}_{\perp}) - \hbar\omega - i\hbar s}, \quad (8)$$

where s is to be taken in the limit of going to $+0$, and $\beta = 1/k_B T$.

We further introduce the expression [cf. Eq. (2)]

$$\varepsilon_2(\mathbf{k}_{\perp} + \mathbf{Q}) - \varepsilon_1(\mathbf{k}_{\perp}) = \hbar\omega_0 + \frac{\hbar^2}{2m^*} \mathbf{Q} \cdot (2\mathbf{k}_{\perp} + \mathbf{Q}), \quad (9)$$

TABLE I. The cases considered.

Case	T (K)	N_S (cm ⁻²)	L_{QW}^* (nm)	Q (cm ⁻¹)
1	300	10 ¹²	50	10 ⁴
2	300	10 ¹²	50	10 ⁵
3	300	10 ¹¹	50	10 ⁴
4	300	10 ¹²	20	10 ⁵

where

$$\hbar\omega_0 = \frac{3\pi^2\hbar^2}{2m^*L_{\text{QW}}^{*2}}, \quad (10)$$

defining an “effective” QW-width given by

$$\frac{3\pi^2\hbar^2}{2m^*L_{\text{QW}}^{*2}} = \frac{3\pi^2\hbar^2}{2m^*L_{\text{QW}}^2} + N_S(A_{21} - B_{21}). \quad (11)$$

This has been done in order to introduce an open parameter to be used for scaling the energy [frequency $z = \omega/\omega_0$ in Eqs. (16)–(22)], and whose value would follow from the data in each experiment. This is necessary to overcome the lack of information on (1) the knowledge of many-body effects present in A and B , i.e., the direct and exchange corrections to the self-consistent energy-band levels, and (2) the effect of the fractal-like structure of the QW interfaces, i.e., the details of their roughness, which is discussed in the second part of Sec. IV.

As noted before, the values of A and B can be derived from the experimental data. Consider the case of Ref. 4,

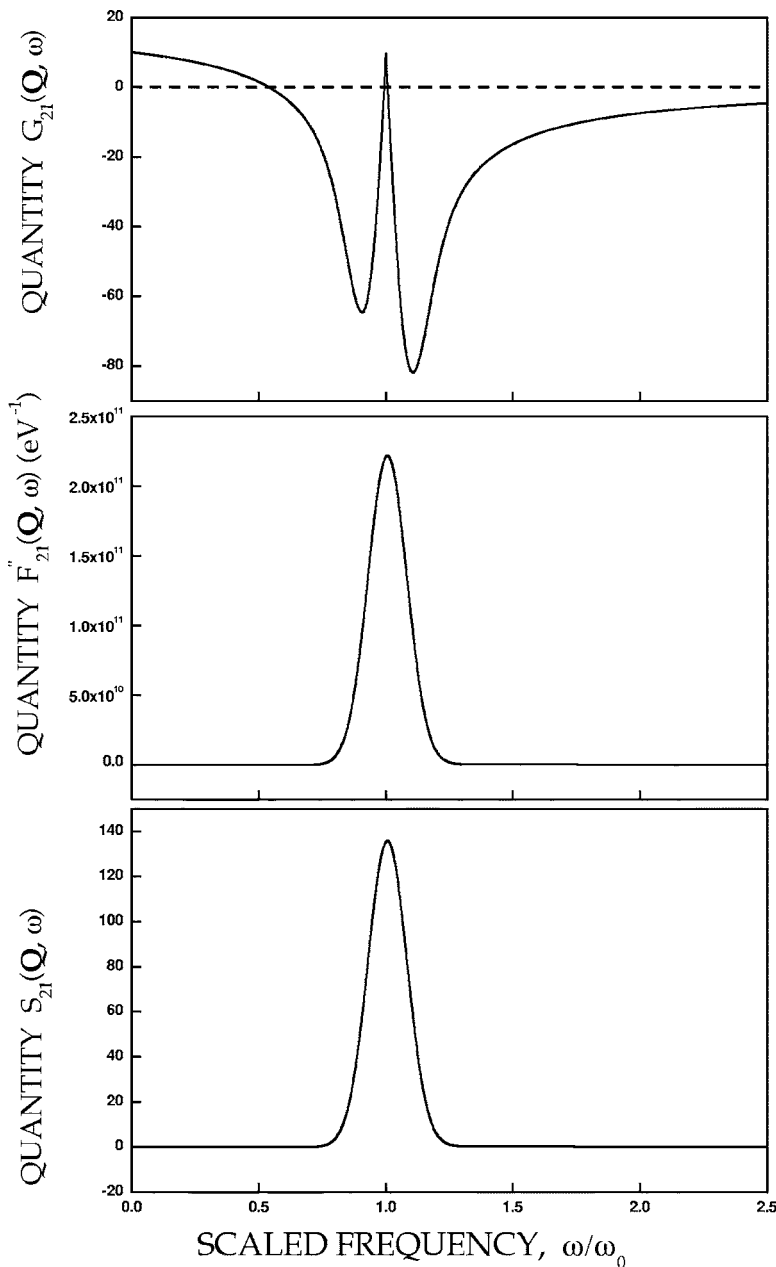


FIG. 1. The quantities $G_{21}(\mathbf{Q}, \omega)$, $F''_{21}(\mathbf{Q}, \omega)$, and $S_{21}(\mathbf{Q}, \omega)$ versus ω/ω_0 in case 1 of Table I. The quantities $G_{21}(\mathbf{Q}, \omega)$ and $S_{21}(\mathbf{Q}, \omega)$ are dimensionless. In the upper figure can be observed the first three roots; the fourth one, at $\omega/\omega_0 \approx 7.380$, is outside the figure.

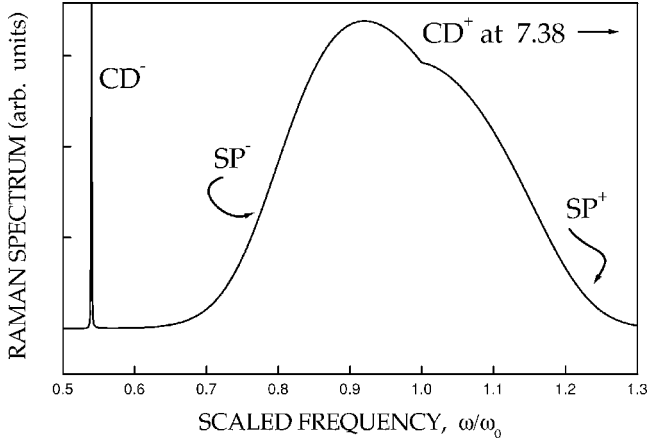


FIG. 2. The Raman spectrum (in arbitrary units) in case 1 of Table I. The narrow band from charge-density excitations, CD^- , and two overlapping broad bands generated by single-particle excitations can be noted. The fourth one due to charge-density excitations, CD^+ , centered at 7.380 is outside the figure.

particularly Fig. 4(a): The difference in frequencies of the peak positions of the bands due to single-particle excitations, with and without spin flip, results in $E_{(SPE)} - E_{(SDW)} = N_S A_{12} \approx (48 - 45) \text{ meV} = 3 \text{ meV}$. On the other hand, from $\hbar\omega_0 = 3\pi^2\hbar^2/2m^*L_{QW}^2 + N_S(A_{12} - B_{12})$ it follows approximately that $48 \text{ meV} = 51 \text{ meV} + (3 \text{ meV} - N_S B_{12})$, and then $N_S B_{12} \approx 6 \text{ meV}$.

Using these values in Eq. (11), we find that $L_{QW}^* \approx 18.5 \text{ nm}$, which is 3% larger than the QW-width of 18 nm, which value also follows directly from Eq. (10), once we accept that $\hbar\omega_0 \approx 48 \text{ meV}$. Using Eq. (9), after neglecting the contribution in Q^2 we find that Eq. (8) takes the form

$$F_{21}(\mathbf{Q}, \omega) = \sum_{\mathbf{k}_\perp} \frac{f_1(\mathbf{k}_\perp) - f_2(\mathbf{k}_\perp + \mathbf{Q})}{\Delta\varepsilon}, \quad (12)$$

where $\Delta\varepsilon = \hbar(\omega_0 - \omega) + (\hbar^2\mathbf{Q} \cdot \mathbf{k}_\perp / m^*) - i\hbar s$. Calling $F'_{21}(\mathbf{Q}, \omega)$ and $F''_{21}(\mathbf{Q}, \omega)$ the real and imaginary parts of $F_{21}(\mathbf{Q}, \omega)$, the scattering cross section of Eq. (7) becomes

$$\frac{d^2\sigma}{d\omega d\Omega} \sim [1 - e^{\beta\hbar\omega}]^{-1} \frac{F''_{21}(\mathbf{Q}, \omega)}{G_{21}^2(\mathbf{Q}, \omega) + S_{21}^2(\mathbf{Q}, \omega)}, \quad (13)$$

where

$$G_{21}(\mathbf{Q}, \omega) = [1 + V_{2D}(\mathbf{Q})F'_{21}(\mathbf{Q}, \omega)]$$

and

$$S_{21}(\mathbf{Q}, \omega) = [V_{2D}(\mathbf{Q})F''_{21}(\mathbf{Q}, \omega)]$$

are dimensionless.

Considering the presence of the distribution functions f_1 and f_2 , in F_{21} , we separate the study into two limiting conditions, namely, the nondegenerate statistical regime and the highly degenerate regime.

A. The nondegenerate regime

This is the regime of high temperature, i.e., $T \gg T_F$, where T_F is the Fermi temperature of the electron system. However it is better characterized by the condition (see, for example, Ref. 15) $n\Lambda_T^3 \ll 1$, where Λ_T is the de Broglie thermal wavelength $\Lambda_T = \hbar / (2m^*k_B T)^{1/2}$. In such circumstances the Fermi-Dirac distributions can be conveniently approximated by Maxwell-Boltzmann distributions, that is

$$f_l(\mathbf{k}_\perp) = C \exp[-\beta\varepsilon_l(\mathbf{k}_\perp)], \quad (14)$$

where

$$C = N_S \frac{\pi\hbar^2}{m^*} \beta \left[\sum_l \exp(-\beta l^2 \hbar\omega_0) \right]^{-1}. \quad (15)$$

After some calculations we find that

$$F'_{21}(\mathbf{Q}, \omega) = \beta N_S S \tilde{C} \left\{ 1 - \sqrt{\pi} \left[\frac{\xi_Q (1 - e^{-\beta\hbar\omega_0})}{\beta\hbar\omega_0} + \xi_Q (z - 1) \right] e^{-\xi_Q^2 (z - 1)^2} \text{Erfi}[\xi_Q |z - 1|] \right\}, \quad (16)$$

where $\text{Erfi}[\xi_Q |z - 1|]$ is the imaginary error function, $\tilde{C} = [\sum_l \exp(-\beta l^2 \hbar\omega_0)]^{-1}$, $z = \omega / \omega_0$, and

$$\xi_Q = \left(\frac{\beta m^* \omega_0^2}{2Q^2} \right)^{1/2}. \quad (17)$$

On the other hand,

$$F''_{21}(\mathbf{Q}, \omega) = \beta N_S S \tilde{C} \left\{ \sqrt{\pi} \left[\frac{\xi_Q (1 - e^{-\beta\hbar\omega_0})}{\beta\hbar\omega_0} + \xi_Q (z - 1) \right] e^{-\xi_Q^2 (z - 1)^2} \right\}. \quad (18)$$

B. The highly-degenerate regime

We consider now the limit of very low temperatures ($T \ll T_F$ or $n\Lambda_T^3 \gg 1$), and we approximate the calculation taking for the Fermi-Dirac populations a Heaviside step function equal to 1 from zero energy to the Fermi level, and zero thereafter. In such conditions we find that

$$F'_{21}(\mathbf{Q}, \omega) = - \left(\frac{m^* S}{\pi\hbar^2 Q} \right) |b(\mathbf{Q}, \omega)|, \quad (19)$$

for $|b(\mathbf{Q}, \omega)| = (m^* \omega_0 / \hbar Q) |z - 1| \leq k_F$,

$$F''_{21}(\mathbf{Q}, \omega) = - \left(\frac{m^* S}{\pi\hbar^2 Q} \right) [|b(\mathbf{Q}, \omega)| - (|b(\mathbf{Q}, \omega)|^2 - k_F^2)^{1/2}], \quad (20)$$

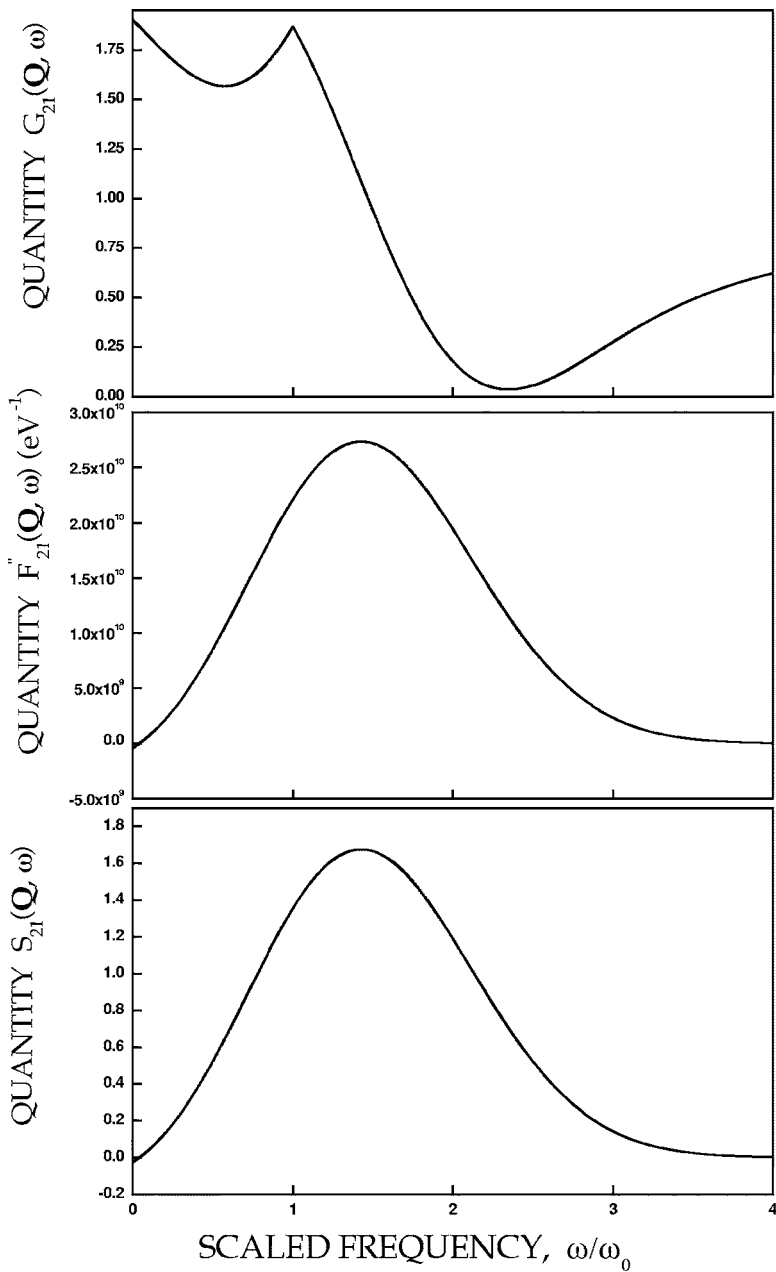


FIG. 3. The quantities $G_{21}(\mathbf{Q}, \omega)F''_{21}(\mathbf{Q}, \omega)$, and $S_{21}(\mathbf{Q}, \omega)$ versus ω/ω_0 in case 2 of Table I. The quantities $G_{21}(\mathbf{Q}, \omega)$ and $S_{21}(\mathbf{Q}, \omega)$ are dimensionless. Quantity $G_{21}(\mathbf{Q}, \omega)$ is always non-null and presenting two dips and one cusp (cf. Fig. 1).

for $|b(\mathbf{Q}, \omega)| > k_F$.

On the other hand,

$$F''_{21}(\mathbf{Q}, \omega) = \left(\frac{m^* S}{\pi \hbar^2 Q} \right) (k_F^2 - |b(\mathbf{Q}, \omega)|^2)^{1/2}, \quad (21)$$

for $|b(\mathbf{Q}, \omega)| \leq k_F$ and

$$F''_{21}(\mathbf{Q}, \omega) = 0, \quad (22)$$

for $|b(\mathbf{Q}, \omega)| > k_F$.

III. RAMAN SPECTRA AND ELEMENTARY EXCITATIONS

To perform numerical calculations we considered the case of a single QW formed by a thin GaAs layer of thickness L_{QW} sandwiched between two larger barriers $\text{Al}_x\text{Ga}_{1-x}\text{As}$

layers. First, we take the *statistical nondegenerate situations*, characterized by Eq. (13) together with Eqs. (16) and (18). In the expression for the scattering cross section of Eq. (13), we shall see that the term $G_{21}(\mathbf{Q}, \omega)$, plays a fundamental role in determining the Raman bands, as is also the case in bulk material. Taking $T=300$ K and considering an electron effective mass $m^*=0.068m_0$ we analyzed several cases characterized by varying values of the sheet-density, N_S , the effective QW width, L_{QW}^* , and wave number \mathbf{Q} . We recall that, on the one hand, $\hbar\mathbf{Q}$ is the momentum transferred in the scattering event, and on the other, that we are dealing with resonant Raman scattering: therefore the photon energy is of the order or slightly larger than the band gap, then, taking $E_G \approx 1.45$ eV, the photon wave number is $\approx 7.3 \times 10^4 \text{ cm}^{-1}$. Consequently in forward scattering we have $Q \approx 1.5 \times 10^5 \text{ cm}^{-1}$, at right angle scattering $Q \approx 10^5 \text{ cm}^{-1}$, and at backscattering $Q \approx 2 \times 10^3 \text{ cm}^{-1}$ (once we take into account

that the Raman shift is on the order of 50 meV). We discuss the four cases indicated in Table I.

Case 1: $N_S=10^{12}$ cm $^{-2}$; $L_{QW}^*=50$ nm; $Q=10^4$ cm $^{-1}$. In Fig. 1 are shown the quantities $G_{21}(\mathbf{Q}, \omega)$, $F_{21}''(\mathbf{Q}, \omega)$, and $S_{21}(\mathbf{Q}, \omega)$ versus the reduced frequency $z=\omega/\omega_0$. We can see in the upper figure the presence of four *roots* (the higher one frequency is not included) at $z \approx 0.546$; 0.992; 1.007, and 7.380. These four *roots* give rise in the Raman spectrum to the four bands corresponding to the four types of excitation of electron system in the QW.

The corresponding Raman spectrum, shown in Fig. 2, presents four bands: as previously noted (see Appendix A), they correspond to a lower collective charge-density excitation, (CD $^-$), at $\omega_{CD}^- \approx 0.546\omega_0$, two overlapping bands corresponding to single particle excitations (SP $^\pm$), centered at $\omega_{SP}^- \approx 0.992\omega_0$ and $\omega_{SP}^+ \approx 1.007\omega_0$, and a fourth band (not shown in the figure) corresponding to an upper collective charge density excitation (CD $^+$) at $\omega_{CD}^+ \approx 7.380\omega_0$.

Case 2: $N_S=10^{12}$ cm $^{-2}$; $L_{QW}^*=50$ nm; $Q=10^5$ cm $^{-1}$. The difference from case 1 is in the value of the wave number Q , here an order of magnitude greater. In Fig. 3 are shown the quantities $G_{21}(\mathbf{Q}, \omega)$, $F_{21}''(\mathbf{Q}, \omega)$, and $S_{21}(\mathbf{Q}, \omega)$ versus ω/ω_0 . In the upper figure is shown that the quantity $G_{21}(\mathbf{Q}, \omega)$ *does not possess zeros*, but has a shape similar to the one of Fig. 1, that is, it *presents two dips and one cusp*. The corresponding Raman spectrum is shown in Fig. 4: two bands centered at approximately the position of the minima of the two expected bands due to single-particle excitations can be observed, while those that would correspond to the collective excitations are not observed (at the scale used here). It can be noticed that such behavior is also characteristic of the spectrum of light scattered from a classical, single component plasma when Q is increased as done here when going from case 1 to case 2.⁶ Also for room temperature, $T=300$ K, we consider now:

Case 3: $N_S=10^{11}$ cm $^{-2}$; $L_{QW}^*=50$ nm; $Q=10^4$ cm $^{-1}$. The difference from case 1 is in the sheet-density, which is an order of magnitude smaller. In Fig. 5 are shown the quantities $G_{21}(\mathbf{Q}, \omega)$, $F_{21}''(\mathbf{Q}, \omega)$, and $S_{21}(\mathbf{Q}, \omega)$ versus ω/ω_0 . We can see in the upper figure the presence of four *roots*, at $z \approx 0.708$; 0.984; 1.015; and 1.651. The corresponding Raman spectrum is presented in Fig. 6, which has a similarity with the one of Fig. 2. The band associated with the lower collective mode, CD $^-$, and two bands due to single-particles, SP $^-$ and SP $^+$, can be noted, while the upper collective mode, CD $^+$, centered at $\omega/\omega_0 \approx 1.651$, is outside the figure.

Case 4: $N_S=10^{12}$ cm $^{-2}$; $L_{QW}^*=20$ nm; $Q=10^5$ cm $^{-1}$. This is similar to case 2, but with reduction in the value of L_{QW}^* . In Fig. 7 are shown the quantities $G_{21}(\mathbf{Q}, \omega)$, $F_{21}''(\mathbf{Q}, \omega)$, and $S_{21}(\mathbf{Q}, \omega)$ versus ω/ω_0 . We can see in the upper figure the presence of four *roots*, at $\omega/\omega_0 \approx 0.676$; 0.963; 1.033; and 2.106, and also two dips and one cusp. The corresponding Raman spectrum is shown in Fig. 8, where a lower frequency broad band corresponding to the lower collective excitation, CD $^-$, which overlaps with the two bands SP $^-$ and SP $^+$ corresponding to single-particle excitations can be noted. The band due to the upper collective excitation, at $\omega/\omega_0 \approx 2.106$, is outside the figure.

Let us consider now the case of very low temperatures,

i.e., the *ultra-degenerate* case of Sec. II B. Using the results indicated in that section, we obtain the roots of the quantity $G_{21}(\mathbf{Q}, \omega)=[1+V_{2D}F'_{21}(\mathbf{Q}, \omega)]$, namely

$$z_{SP}^\pm = \frac{\omega_{SP}^\pm}{\omega_0} = 1 \mp \left(\frac{4\hbar^2 \varepsilon_0}{\pi e^2 m^*} \right) L_{QW}^{*2} Q^3, \quad (23)$$

for

$$(e^2 m^* / \varepsilon_0 \hbar^2 Q^2) (N_S / 2\pi)^{1/2} > 1$$

[i.e., $|b(\mathbf{Q}, \omega)| < k_F$, corresponding to $\hbar\omega$ inside the continuum of single-electron excitations; see Fig. 9] which are the peak positions of the bands that in the spectrum correspond to scattering by single particles. It can be noted that the separation of the two lines is

$$(8\hbar^2 \varepsilon_0 / \pi e^2 m^*) L_{QW}^{*2} Q^3.$$

On the other hand, the two other roots correspond to the bands arising out of scattering by the collective modes, and are

$$z_{CD}^\pm = \frac{\omega_{CD}^\pm}{\omega_0} = 1 \mp \frac{1}{2} \left(\frac{4\hbar^2 \varepsilon_0}{\pi e^2 m^*} \right) L_{QW}^{*2} Q^3 \left[1 + \frac{N_S}{2\pi} (e^2 m^* / \varepsilon_0 \hbar^2 Q^2)^2 \right], \quad (24)$$

for

$$\frac{(2e^2 m^* / \varepsilon_0 \hbar^2 Q^2) (N_S / 2\pi)^{1/2}}{\left[1 + \frac{N_S}{2\pi} (e^2 m^* / \varepsilon_0 \hbar^2 Q^2)^2 \right]} < 1$$

[i.e., $|b(\mathbf{Q}, \omega)| > k_F$, corresponding to $\hbar\omega$ outside the continuum of single-electron excitations, see Fig. 9].

In Table II we indicate, for each set of values of the sheet density N_S , the effective QW width L_{QW}^* and the wave num-

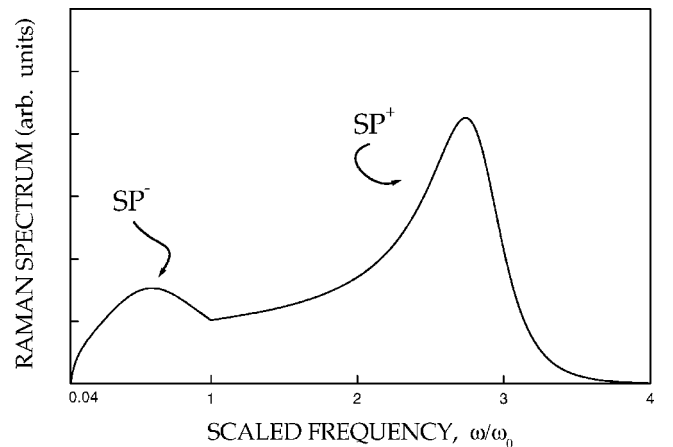


FIG. 4. The Raman spectrum (in arbitrary units) in case 2 of Table I. Two wide bands corresponding to single-particle excitations can be observed. The two bands due to collective excitations, CD $^-$, and CD $^+$ are practically unnoticeable.

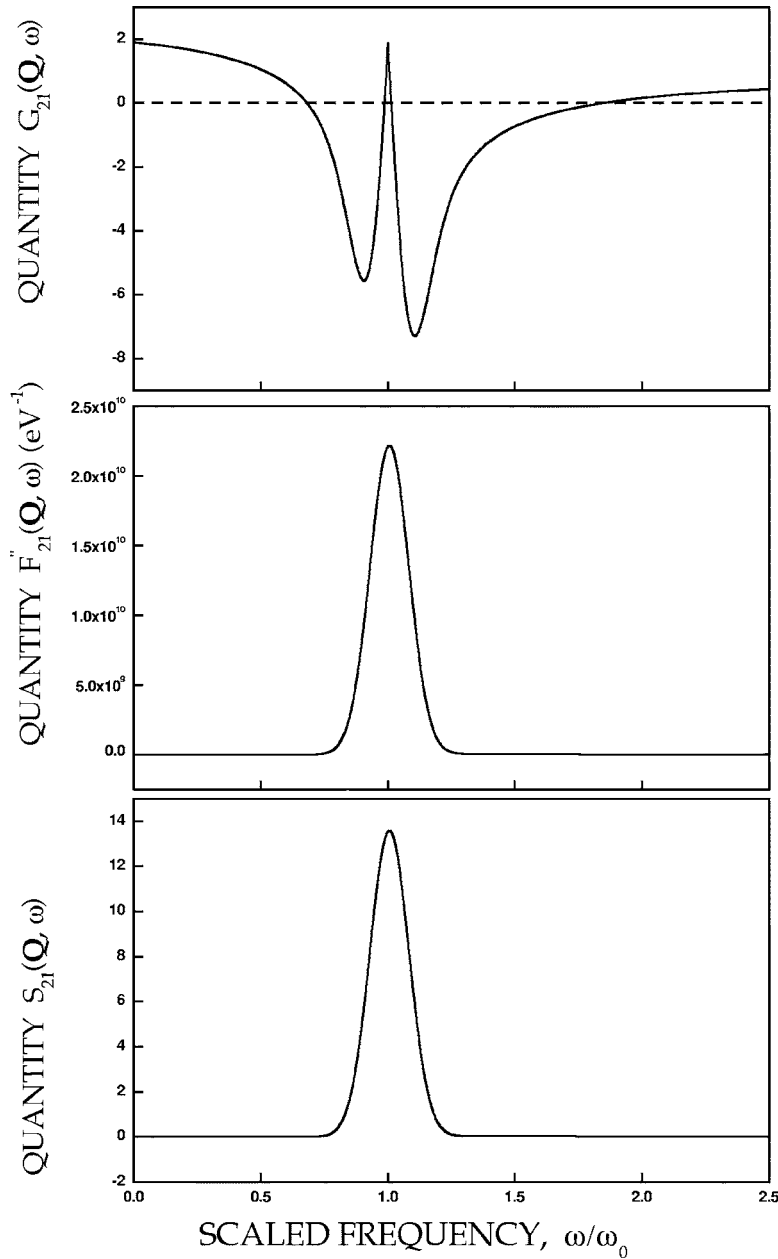


FIG. 5. The quantities $G_{21}(\mathbf{Q}, \omega)$, $F''_{21}(\mathbf{Q}, \omega)$, and $S_{21}(\mathbf{Q}, \omega)$ versus ω/ω_0 in case 3 of Table I. The quantities $G_{21}(\mathbf{Q}, \omega)$ and $S_{21}(\mathbf{Q}, \omega)$ are dimensionless. The presence of the four roots in $G_{21}(\mathbf{Q}, \omega)$ can be noted.

ber Q , the position of the roots of $G_{21}(\mathbf{Q}, \omega)$ in units of ω_0 , corresponding to the single particles and the upper charge density: in all the cases presented the one associated with the lower charge density is forbidden, and the two associated with the single particles are in practically near coincidence. Therefore, the Raman spectrum presents only two bands centered at the position of such roots. In the experiment of Ref. 4 the quantities involved are $N_S \approx 6.3 \times 10^{11} \text{ cm}^{-2}$, $L_{\text{QW}} \approx 18 \text{ nm}$, $\omega_0 \approx 47 \text{ meV}$, then the effective QW width we have introduced is $\sim 10 \text{ nm}$, and the correction to the self-consistent energy levels, i.e., $N_S(A_{21} - B_{21})$, is approximately -3 meV , moreover, $Q \approx 10^4 \text{ cm}^{-1}$, and $T_0 \approx 12 \text{ K}$. Using these values in the highly degenerate regime (i.e., taking $T_0 \approx 0 \text{ K}$ instead of the intermediate condition at $T_0 \approx 12 \text{ K}$), we show in Fig. 10 the calculated Raman spectrum. As already anticipated there are only two bands, corresponding to those observed in the experiment: one consisting of the two

overlapping bands due to single-particle excitations, and one associated with the upper collective charge density excitation. It can be noted that the separation of both lines is nearly $7.8\omega_0$, whereas the separation observed in the experiment is nearly $1.3\omega_0$. This difference can be ascribed to the use of a Fermi-Dirac step-function distribution, corresponding to the ultra-degenerate limit, while in the experiment the temperature is $T_0 = 12 \text{ K}$ corresponding to an intermediate degenerate regime. Comparing results that we have obtained in the same conditions but with temperatures 0 and 50 K, it can be noted that the difference is in fact reduced.

IV. CONCLUDING REMARKS

We have presented a theoretical study of Raman resonant scattering by mobile electrons populating the two-lowest conduction subbands of quantum wells in heterostructures of

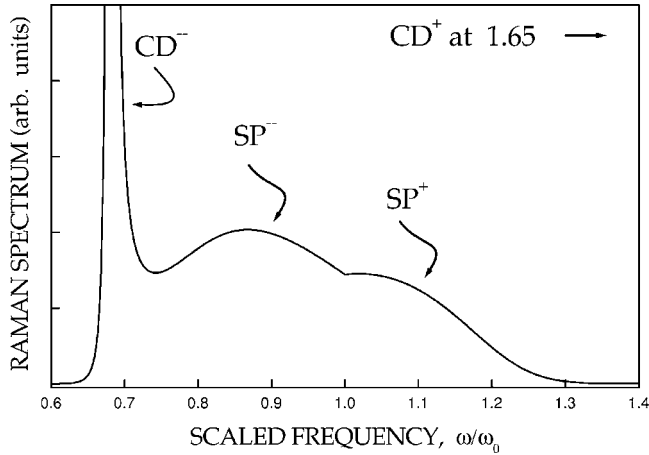


FIG. 6. The Raman spectrum in case 3 of Table I. The band from charge-density excitations, CD^- , and the two overlapping bands associated with single-particle excitations, SP^- and SP^+ , can be observed. The higher-in-frequency band due to collective excitations, CD^+ , is outside the figure.

polar semiconductors. This kind of experiment (experimental data are available in Refs. 3 and 4) reveals the spectrum of elementary excitations, which is composed of single-particle excitations and collective modes. It has been shown that the spectrum should display four bands: two of them correspond to transitions between states in the continuum of single-particle excitations (one for particles with group velocity in the direction of the momentum transfer in the scattering event, and the other for those with opposed group velocity; see Appendix A). The other two excitations are of a collective character—plasmon-like charge density oscillations—with bands centered at frequencies below and above those in the bands associated with the single-particle excitations. As noted in Sec. I we have here a situation similar to the one that is present in the Raman spectrum of a double-photoinjected plasma in bulk semiconductors.^{9,10}

Moreover, as has been shown, the Raman spectrum is strongly dependent on several characteristics of the sample and on the experimental protocol. We stress that notable differences show up in the relative positioning of the bands, and their relative intensities; bands may be prohibited by the effect of momentum and energy conservation laws. This is a consequence of the strong influences, in each experiment, of the momentum transfer $\hbar\mathbf{Q}$ (dependent on the laser photon frequency and the experimental geometry), the QW width, the density of carriers, and the temperature. Evidently this permits the consideration of an enormous number of situations, and in Sec. III we have presented a few examples (see Figs. 2, 4, 6, 8, and 9), and discussed each one.

Finally, we would like to add a brief comment, related to the fact that the growth of quantum wells in heterostructures produces fractal-like structured interfaces, as an inevitable result.¹⁶ Thus, such roughness, which, in the case of very narrow QWs (say, widths up to ≈ 10 nm) is on the same scale as the nanometric-scale QW width, can greatly affect the physical (optical, transport, etc.) properties in these systems. In such cases, the roughness of the boundaries needs to be taken into account since it can act as a strong scatterer. An

illustrative calculation corresponding to a computationally modeled QW was reported by Runge and Zimmermann.¹⁷ They apply their results to the study of absorption and luminescence in QWs, showing that “anomalous” results are to be expected (that is, different from the result obtained for the ideal QW of quite smooth interfaces). The characterization of the “quality” of the interfaces—in the sense of deviation from the smooth interfaces with fractal dimension two to fractional dimensions smaller than two—by means of optical spectroscopy is reported in Ref. 18. The fractal aspects of the question are discussed in Ref. 19, where, for the analysis of the data, the use of an unconventional statistical mechanics²⁰ in the Renyi approach²¹ is considered.

Interface structural properties in quantum wells have been extensively investigated, as they are extremely important in the high performance of electronic and optoelectronic QW-based devices.²² Direct observations of the interfacial characteristics have been obtained by scanning tunneling microscopy, atomic force microscopy, and transmission electron microscopy.²³ Besides the optical characterization using photoluminescence,¹⁸ another optical measurement can be the resonant Raman scattering considered here. However, we have not introduced a treatment that can give information on the fractal dimension of the interfaces as done in Ref. 18 since we have considered not very narrow QWs, i.e., widths larger than 10 nm. As shown in Ref. 18, the influence on the results of the fractal subnanometric inhomogeneities on the interfaces is less and less effective as the QW-width increases. This is a consequence of L_{QW} becoming order(s) of magnitude larger than the homogeneities on the interfaces.

ACKNOWLEDGMENTS

The authors would like to acknowledge the financial support received from the São Paulo State Research Foundation, FAPESP (ARV, RL), and Mato Grosso do Sul State Research Foundation, FUNDECT (AAPS). We thank E. A. Meneses (IFGW-Unicamp) for calling our attention to this problem and for useful discussions.

APPENDIX A: THE EXCITATION DIAGRAM

Let us consider the excitation spectrum of the electrons involving the lowest two sub-bands. The single-particle transitions are

$$(1, \pm k_x, k_y) \rightarrow (2, \pm k_x + Q, k_y), \quad (\text{A1})$$

where we have taken the \mathbf{x} axis in the direction of the momentum transfer \mathbf{Q} . These transitions are illustrated in Fig. 11, where we can see the differences between the cases when the group velocity of the electron is in the direction of \mathbf{Q} and when it is in the opposite direction, but which corresponds to the same kinetic energy $\hbar^2 k_{\perp}^2 / 2m^*$. Moreover, the quantity

$$F'_{21}(\mathbf{Q}, \omega) = \sum_{\mathbf{k}_{\perp}} \frac{\Theta(k_{\perp} - k_F)}{\hbar\omega_0 - \hbar\omega + (\hbar^2/m^*)k_x Q}, \quad (\text{A2})$$

corresponding to the pure quantum state, i.e., Eq. (12) at $T_0=0$ K and subband $l=1$ partially occupied, has poles at the

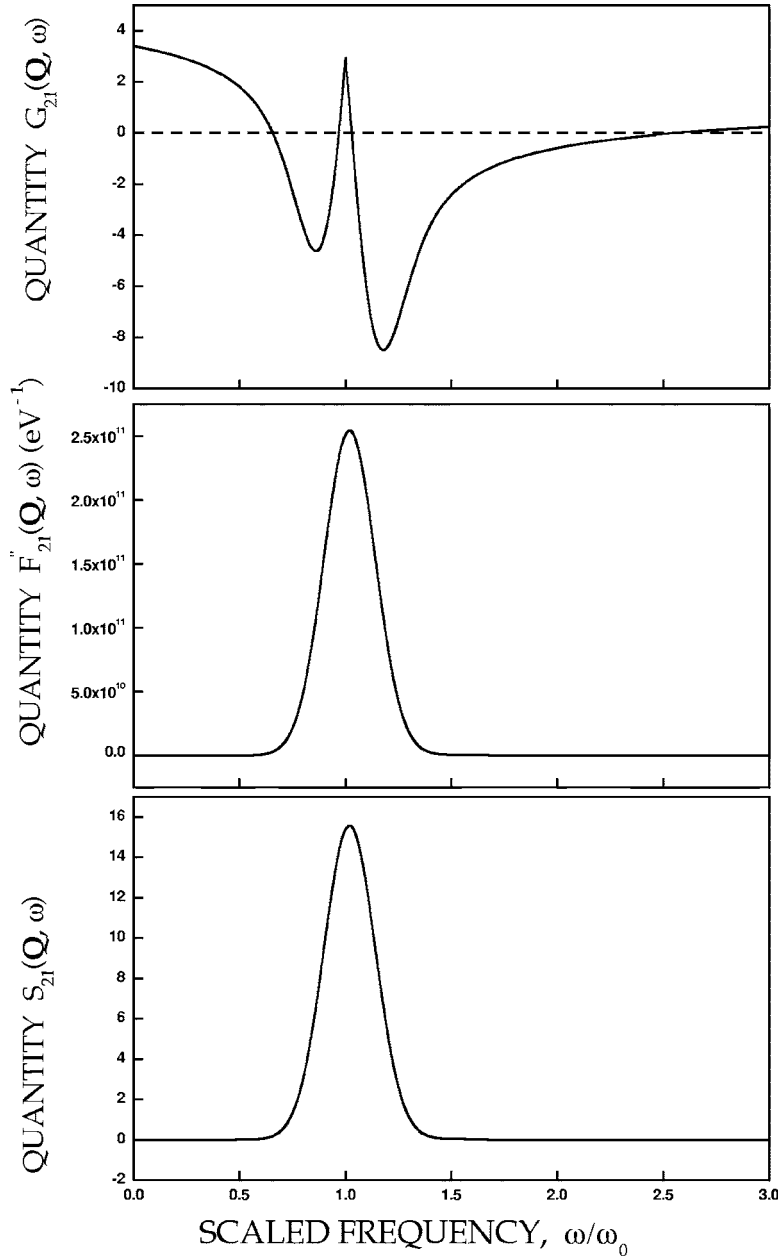


FIG. 7. The quantities $G_{21}(\mathbf{Q}, \omega)$, $F'_{21}(\mathbf{Q}, \omega)$, and $S_{21}(\mathbf{Q}, \omega)$ versus ω/ω_0 in case 4 of Table I. The quantities $G_{21}(\mathbf{Q}, \omega)$ and $S_{21}(\mathbf{Q}, \omega)$ are dimensionless. The four roots are present in $G_{21}(\mathbf{Q}, \omega)$.

single-particle excitation energies in units of $\hbar\omega_0$, $z = \omega/\omega_0$, in the continuum indicated by the full segment in the interval between $1 - \hbar k_F Q/m^* \omega_0$ and $1 + \hbar k_F Q/m^* \omega_0$, and it has the form shown in Fig. 9 (we have used $Q = 10^5 \text{ cm}^{-1}$, $\hbar\omega_0 = 47 \text{ meV}$). The intersection of $F'_{21}(\mathbf{Q})$ with $-1/V_{2D}(Q)$ —providing the zeros of $G_{21}(\mathbf{Q}, \omega)$ in this case—completes the spectrum of excitations indicating the position of the energies of the collective modes, the lower one CD^- and the upper one CD^+ corresponding to charge density (plasmon-like) oscillations. As noted in the main text, there is in fact no intersection on the low frequency side of the figure, indicating that, in this case, the low-frequency collective excitation is forbidden.

APPENDIX B: THE SCATTERING CROSS SECTION

The differential cross section for scattering of a flux of incident photons with momentum $\hbar\mathbf{k}_L$ and energy $\hbar\omega_L$, pro-

ducing scattered photons with momentum $\hbar\mathbf{k}_S$ —implying a momentum transfer $\hbar\mathbf{Q} = \hbar\mathbf{k}_L - \hbar\mathbf{k}_S$ —and energy $\hbar\omega_S$, and thus the energy transfer being $\hbar\omega = \hbar\omega_L - \hbar\omega_S$, is given by the number of photons that enter the detector in a solid angle $d\Omega$ per unit of time divided by the flux of incident particles. In a calculation of all orders in perturbation theory it follows that (e.g., Ref. 24).

$$\frac{d^2\sigma}{d\Omega d\omega} \sim \int_{-\infty}^{\infty} d\tau e^{-i\omega\tau} \text{Tr}\{\tilde{\mathfrak{R}}_{\mathbf{Q}}^\dagger(\tau)\tilde{\mathfrak{R}}_{\mathbf{Q}}(\tau)\rho_{\text{gc}}\}, \quad (\text{B1})$$

where operator $\tilde{\mathfrak{R}}(\tau)$ —given in the interaction representation—satisfies the integral equation

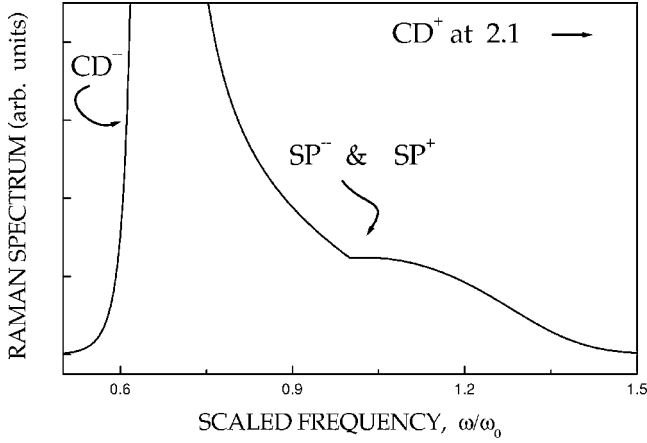


FIG. 8. The Raman spectrum in case 4 of Table II. The band from charge-density excitations, CD^- , the two overlapping bands associated with single-particle excitations, SP^- and SP^+ , can be observed. The higher-in-frequency band due to collective excitations, CD^+ , is outside the figure.

$$\tilde{\mathfrak{R}}_{\mathbf{Q}}(t) = \tilde{\mathbf{V}}_{\mathbf{Q}}(t) \left[1 + \frac{1}{i\hbar} \int_{-\infty}^t dt' \tilde{\mathfrak{R}}_{\mathbf{Q}}(t') \right], \quad (\text{B2})$$

with $\tilde{\mathbf{V}}(t)$ being the interaction potential, that of the electrons with the electromagnetic field in the case considered here, and ρ_{gc} being the grand-canonical statistical operator. Index \mathbf{Q} indicates that the matrix element between the incident plane-wave state $|\mathbf{k}_L\rangle$ and the scattered plane-wave state $|\mathbf{k}_S\rangle$, of the photons has been used. It can be noted that Eq. (B2) permits a solution by iteration, to obtain

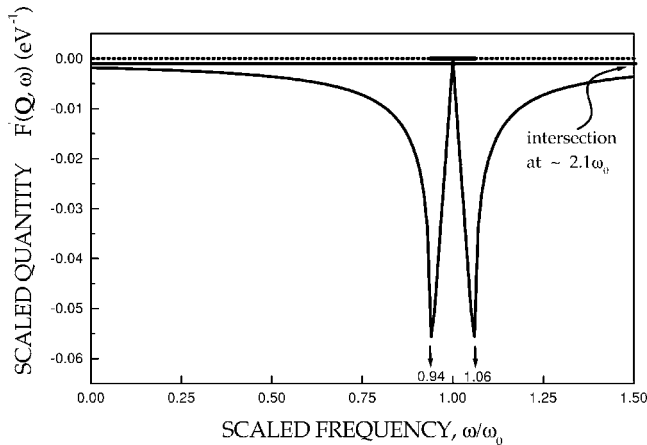


FIG. 9. Quantity $F'_{21}(\mathbf{Q}, \omega)$ of Eqs. (19) and (20), in scaled units versus the scaled frequency ω/ω_0 . The blackened segment (in the interval 0.94–1.06) corresponds to the continuum of single-electron excitations. $Q=10^5 \text{ cm}^{-1}$, $N_S=10^{12} \text{ cm}^{-2}$, $\hbar\omega_0=47 \text{ meV}$, $L_{\text{QW}}^*=10 \text{ nm}$ were used. The intersections of the figure with the horizontal full line corresponds to the zeros of $G_{21}(\mathbf{Q}, \omega)$: the two associated with single-electron excitations around $\omega=\omega_0$ and the upper collective excitation at $\omega \approx 2.1\omega_0$, outside the figure; the lower collective excitation is forbidden.

TABLE II. Roots of $G_{21}(\mathbf{Q}, \omega)$.

$N_S \text{ (cm}^{-2}\text{)}$	$L_{\text{QW}}^* \text{ (nm)}$	$Q \text{ (cm}^{-1}\text{)}$	$SP^\pm(\omega_0)$	$CD^+(\omega_0)$
10^{11}	20	10^4	≈ 1	≈ 5.3
10^{11}	10	10^4	≈ 1	≈ 2.1
10^{11}	10	10^5	≈ 1	≈ 1.1
10^{11}	50	10^4	≈ 1	≈ 27.9
10^{12}	10	10^5	≈ 1	≈ 2.1
10^{12}	20	10^5	≈ 1	≈ 5.3
10^{12}	20	10^4	≈ 1	≈ 44.1
10^{12}	10	10^4	≈ 1	≈ 11.8
10^{12}	50	10^4	≈ 1	≈ 270.4

$$\tilde{\mathfrak{R}}_{\mathbf{Q}}(t) = \tilde{\mathbf{V}}_{\mathbf{Q}}(t) \left\{ 1 + \frac{1}{i\hbar} \int_{-\infty}^t dt' \tilde{\mathbf{V}}_{\mathbf{Q}}(t') + \left(\frac{1}{i\hbar} \right)^2 \times \int_{-\infty}^t dt' \tilde{\mathbf{V}}_{\mathbf{Q}}(t') \int_{-\infty}^{t'} dt'' \tilde{\mathbf{V}}_{\mathbf{Q}}(t'') + \dots \right\}, \quad (\text{B3})$$

a Born series in perturbation theory involving the interaction in all orders.

The case of the interaction potential between the electrons and the electromagnetic field—of vector potential \mathbf{A} —contains two types of contributions involving the coupling of electron charge density with the electromagnetic field, associated with terms containing the scalar product $\mathbf{A}_L \cdot \mathbf{A}_S$ and terms with the presence of $\mathbf{A}_L \cdot \mathbf{p}$ and $\mathbf{A}_S \cdot \mathbf{p}$ (\mathbf{p} is the electron momentum operator). The first produces scattering in first order in Eq. (B1), while the second must go to second order. The former contribution is lost in the background coming out of the barriers, but the second can be detected in resonant scattering, when a photon energy $\hbar\omega_L$ nearing, or slightly exceeding the band gap energy is used. The resulting cross section is proportional to the electron charge density fluctuation, and after use of the usual fluctuation-dissipation theorem in the linear regime around equilibrium, as is the case here (we recall that for systems in a nonlinear regime out of equilibrium a generalized FDT appropriate to such conditions should apply; see Chap. 5 in Ref. 20 and a direct application in Ref. 26), it follows that (e.g., Refs. 6 and 25)

$$d^2\sigma \sim |M(\omega)|^2 (n_\omega + 1) \text{Im} \langle \langle \hat{\rho}_{\mathbf{Q}} | \hat{\rho}_{\mathbf{Q}}^\dagger | \omega \rangle \rangle, \quad (\text{B4})$$

where $\langle \langle \dots \rangle \rangle$ indicates the Fourier transform in time and space of the corresponding Green function involving the charge density $\hat{\rho}$, $n_\omega = [\exp(\hbar\omega/k_B T) - 1]^{-1}$ (then $n_\omega + 1 = [1 - \exp(-\hbar\omega/k_B T)]^{-1}$), and

$$|M(\omega)|^2 = \left| \frac{M_{\text{LS}}}{(E_G + E_{11}^{cv} - \hbar\omega_S)} \right|^2, \quad (\text{B5})$$

at the zone center: E_{11}^{cv} is the sum of the energies of the lowest level in the conduction, with the upper one being in the valence band in the QW and the term M_{LS} corresponding

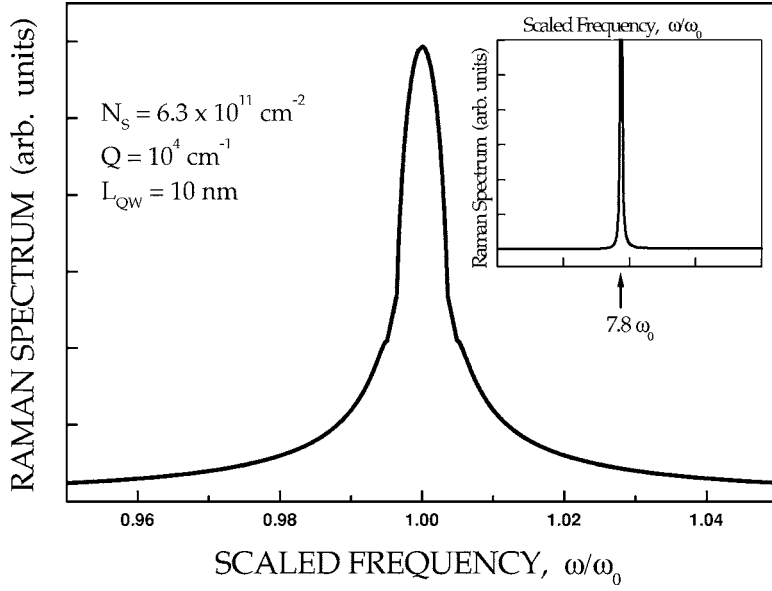


FIG. 10. The Raman spectrum (in arbitrary units) in conditions similar to that of the experiment of Ref. 4. It can be noticed that there are only two bands, corresponding to those observed in the experiment: They consist of the two overlapping bands due to single-particle excitations, and the one associated with the upper collective charge density excitation, indicated in the upper right inset. It can be noted that the separation of both lines is nearly $7.8\omega_0$ indicated by the arrow.

to $M_{LS} = \langle 1c | \mathbf{A}_L \cdot \mathbf{p} | 1v \rangle \langle 1v | \mathbf{A}_S \cdot \mathbf{p} | 1c \rangle$. In Eq. (B5) a pole is present at $\hbar\omega = E_G + E_{11}^{cv} - \hbar\omega_L$ (once $\omega_L = \omega + \omega_S$), characterizing the resonant scattering. When considering the transitions between the levels $l=1$ and $l=2$ in the conduction band in the scattering event, the calculation of the Green function (dealing with Coulomb interaction in RPA) leads to the result of Eq. (7).

It can be noted that Eq. (B4) is the expression for the differential cross section in Raman scattering by electrons,²⁵ with the amplitude M and the Green function to be calculated for each particular case. The Fourier transform of the charge density is given by

$$\hat{\rho}_{\mathbf{Q}} = \sum_{n\mathbf{k}_{\perp}} C_n^{\dagger}(\mathbf{k}_{\perp} + \mathbf{Q}) C_n(\mathbf{k}_{\perp}), \quad (\text{B6})$$

in the case of the electrons in the QW. On the other hand the equation for the Green function is²⁷

$$\hbar\omega \langle \langle \hat{\rho}_{\mathbf{Q}} | \hat{\rho}_{\mathbf{Q}}^{\dagger}; \omega \rangle \rangle = \frac{1}{2\pi} \langle [\hat{\rho}_{\mathbf{Q}}, \hat{\rho}_{\mathbf{Q}}^{\dagger}] \rangle + \langle \langle [\hat{\rho}_{\mathbf{Q}}, \hat{H}] | \hat{\rho}_{\mathbf{Q}}^{\dagger}; \omega \rangle \rangle, \quad (\text{B7})$$

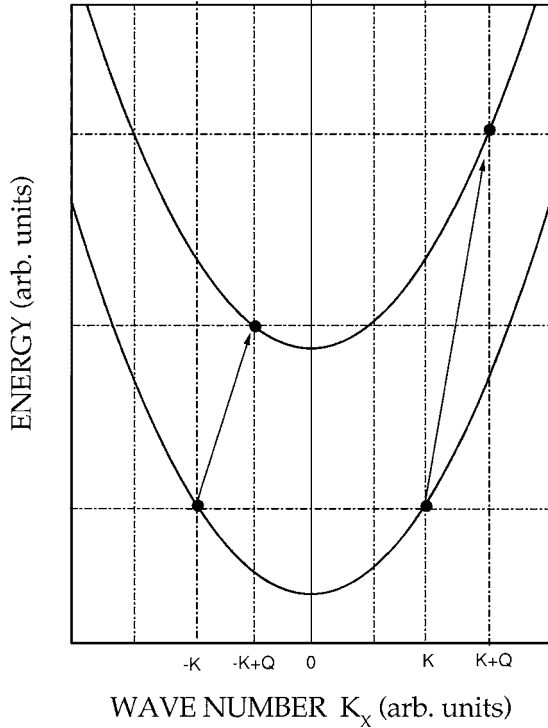


FIG. 11. Schematic representation of the single-electron transitions $(1, \pm k_x, k_y)$ to $(2, \pm k_x + Q, k_y)$.

where $\langle \langle \hat{A} | \hat{B}; \omega \rangle \rangle$ is the Fourier transform in time of the Green function of quantities \hat{A} and \hat{B} , \hat{H} is the system Hamiltonian, and $\langle \dots \rangle$ indicates average value over the equilibrium grand ensemble.

The calculation follows in the same way as is usual for the 3D case, except that interpretation of the index \mathbf{k} in 3D is replaced by $n\mathbf{k}_{\perp}$, the indexes of the electrons in the QW. The final result is²⁵

$$[1 - V_{\mathbf{Q}} L(\mathbf{Q}, \omega)] G(\mathbf{Q}, \omega) - \frac{1}{2\pi} L(\mathbf{Q}, \omega) = 0, \quad (\text{B8})$$

where

$$L(\mathbf{Q}, \omega) = \sum_{n, n', \mathbf{k}_{\perp}} \frac{f_n(\mathbf{k}_{\perp}) - f_{n'}(\mathbf{k}_{\perp} + \mathbf{Q})}{\varepsilon_{n'}(\mathbf{k}_{\perp} + \mathbf{Q}) - \varepsilon_n(\mathbf{k}_{\perp}) - \hbar\omega - i\hbar s}, \quad (\text{B9})$$

and G is the Green function of Eq. (B7).

When we restrict the calculation to include only the two lowest levels ($n=1$ and $n'=2$) the results of Eqs. (8)–(18) follow.

*Electronic address: antonio@dfi.ufms.br

†URL: <http://www.ifi.unicamp.br/~aurea>; electronic address: rlgmesd@ifi.unicamp.br

- ¹A. A. Sirenko, M. K. Zundel, T. Ruf, K. Eberl, and M. Cardona, *Phys. Rev. B* **58**, 12633 (1998).
- ²M. Sasseti, F. Napoli, and B. Kramer, *Eur. Phys. J. B* **11**, 634 (1999).
- ³A. Pinczuk, S. Schmitt-Rink, G. Danan, J. P. Valladares, L. N. Pfeiffer, and K. W. West, *Phys. Rev. Lett.* **63**, 1633 (1989).
- ⁴T. Unuma *et al.*, *Phys. Rev. B* **70**, 153305 (2004).
- ⁵H. C. Liu *et al.*, *Appl. Phys. Lett.* **78**, 3580 (2001).
- ⁶P. A. Wolff, in *Light Scattering in Solids I*, edited by G. B. Wright (Springer, New York, 1969), pp. 273–284.
- ⁷A. Mooradian, in *Light Scattering in Solids I* (Ref. 6), pp. 285–296.
- ⁸D. C. Hamilton and A. L. McWhorter, in *Light Scattering in Solids I* (Ref. 6), pp. 309–316.
- ⁹D. Pines, *Can. J. Phys.* **34**, 1379 (1956); P. Nozières and D. Pines, *Phys. Rev.* **109**, 741 (1958); **109**, 762 (1958); **109**, 1062 (1958); D. Pines and J. R. Schrieffer, *ibid.* **124**, 1387 (1961); P. M. Platzmann, *Phys. Rev.* **139**, A379 (1965); A. Pinczuk, J. Shah, and P. A. Wolff, *Phys. Rev. Lett.* **47**, 1487 (1981).
- ¹⁰A. R. Vasconcellos, R. Luzzi, and A. S. Esperidião, *Phys. Rev. B* **52**, 5021 (1995).
- ¹¹T. Ando, A. B. Fowler, and F. Stern, *Rev. Mod. Phys.* **54**, 437 (1982).
- ¹²L. Hedin and S. Lundquist, in *Solid State Physics Series*, Vol. 23, edited by F. Seitz, D. Turnbull, and H. Ehrenreich (Academic, New York, 1969); L. Hedin, *Phys. Rev.* **139**, A796 (1965).
- ¹³D. Pines and P. Nozières, *The Theory of Quantum Liquids*, Vol. 1 (Benjamin, New York, 1966).
- ¹⁴D. K. Ferry and S. M. Goodnick, *Transport in Nanostructures* (Cambridge University Press, Cambridge, UK, 1997).
- ¹⁵R. K. Pathria, *Statistical Mechanics* (Pergamon, New York, 1972).
- ¹⁶*Dynamics of Fractal Surfaces*, edited by F. Family and T. Viczek (World Scientific, Singapore, 1991).
- ¹⁷E. Runge and R. Zimmermann, *Adv. Solid State Phys.* **38**, 251 (1998).
- ¹⁸E. Laureto, A. R. Vasconcellos, E. A. Meneses, and R. Luzzi, *Int. J. Mod. Phys. B* **18**, 1743 (2004).
- ¹⁹A. R. Vasconcellos, E. Laureto, E. A. Meneses, and R. Luzzi, *Chaos, Solitons Fractals* **28**, 8 (2006).
- ²⁰R. Luzzi, A. R. Vasconcellos, and J. G. Ramos, *cond-mat/0306217*; *cond-mat/0306247*; *Physica A* **340** 163 (2004); *Predictive Statistical Mechanics: A Nonequilibrium Statistical Ensemble Formalism* (Kluwer Academic, Dordrecht, The Netherlands, 2000), Chap. 1, Sec. 3; *Science* **298**, 1171 (2002).
- ²¹A. Renyi, *Probability Theory* (North Holland, Amsterdam, The Netherlands, 1970): see Chap. IX, p. 579 et seq.; P. Jizba and T. Arimitsu, *Ann. Phys. (N.Y.)* **312**, 17 (2004).
- ²²P. Borri *et al.*, *J. Appl. Phys.* **80**, 3011 (1996); K. Fujiwara, K. Kanamoto, and N. Tsukada, *Phys. Rev. B* **40**, 9698 (1989).
- ²³U. Jahn *et al.*, *Phys. Rev. B* **54**, 2733 (1996).
- ²⁴P. Roman, *Advanced Quantum Theory* (Addison-Wesley, Reading, MA, 1965); J. M. Ziman, *Elements of Advanced Theory* (Cambridge University Press, London, UK, 1969).
- ²⁵A. R. Vasconcellos and R. Luzzi, *Nuovo Cimento Soc. Ital. Fis., B* **23**, 335 (1974); *Solid State Commun.* **17**, 510 (1975); *Phys. Rev. B* **14**, 3532 (1976).
- ²⁶A. V. Andrade Neto, A. R. Vasconcellos, and R. Luzzi, *Appl. Phys. Lett.* **85**, 4055 (2004).
- ²⁷D. N. Zubarev, *Nonequilibrium Statistical Thermodynamics* (Consultants Bureau, New York, 1974).